

GEOPHYSICS

Absence of ice-bonded permafrost beneath an Arctic lagoon revealed by electrical geophysics

Micaela N. Pedrazas^{1*}, M. Bayani Cardenas¹, Cansu Demir¹, Jeffery A. Watson¹,
Craig T. Connolly², James W. McClelland²

Relict permafrost is ubiquitous throughout the Arctic coastal shelf, but little is known about it near shore. The presence and thawing of subsea permafrost are vital information because permafrost stores an atmosphere's worth of carbon and protects against coastal erosion. Through electrical resistivity imaging across a lagoon on the Alaska Beaufort Sea coast in summer, we found that the subsurface is not ice-bonded down to ~20 m continually from within the lagoon, across the beach, and underneath an ice-wedge polygon on the tundra. This contrasts with the broadly held idea of a gently sloping ice-bonded permafrost table extending from land to offshore. The extensive unfrozen zone is a marine talik connected to on-land cryopeg. This zone is a potential source and conduit for water and dissolved organic matter, is vulnerable to physical degradation, and is liable to changes in biogeochemical processes that affect carbon cycling and climate feedbacks.

INTRODUCTION

Sea level rise after the Last Glacial Maximum submerged millions of square kilometers of Arctic terrestrial permafrost (1). This relict permafrost beneath the ocean is a major organic carbon stock holding the equivalent of all terrestrial permafrost in the Arctic (2). Just the top 3 m of the Arctic continental shelf is estimated to store ~220 Pg of organic carbon, which is roughly a quarter of the carbon currently held in the atmosphere (3). Subsea ice-bearing permafrost in the Arctic, which nominally extends to the 25-m isobath, has been thawing since the Pleistocene when sea level was 120 m lower (4–6). In particular, the subsea permafrost table has been deepening at an average of 4 cm/year beneath the Alaskan Beaufort Sea (7, 8), but at higher rates of 14 cm/year near Muostakh Island in the Laptev Sea (7, 8) and 25 cm/year in the Bykovsky Peninsula region of Siberia (9). The ongoing thaw and degradation of subsea permafrost have far-reaching effects, but perhaps none is more important than the mobilization of ancient carbon and subsequent release of carbon dioxide and methane, which has the potential to exacerbate global warming (10, 11). The degradation of relict permafrost and its local effects are even more marked adjacent to the coast, where the connection to degrading permafrost on land is even stronger. Determining the extent and thawing of subsea permafrost is imperative.

As a consequence of subsea permafrost degradation, there is a greater transfer of heat between thawed underwater sediment and the frozen coast, potentially facilitating coastal erosion. Thawing and collapsing Arctic coastlines can have erosion rates as high as 25 m/year, releasing 14 Tg of organic carbon annually into the near-shore zones (12). Thaw-induced damage is markedly felt by communities throughout the Arctic and Boreal regions (13). Such is the case in our study area near the village of Kaktovik on Barter Island, a coastal indigenous community located in the continuous permafrost region of the Alaska Beaufort Sea, whose subsistence and cultural identity is intricately connected to their environment. Adjacent to Barter Island is Kaktovik Lagoon, a typical lagoon separated by a barrier island from the Beaufort Sea. Nearly all of Kaktovik Lagoon's

coast is eroding (14). The average coastal erosion rate for this lagoon is 0.6 m/year for the period of 1947–2010, with a maximum rate of 4.5 m/year. Kaktovik Lagoon's coastal retreat exposes terrestrial permafrost, which then becomes inundated. Such resultant subsea permafrost is expected to warm and thaw at an accelerated rate, as coastal waters heat up and experience shorter and shorter periods of ice cover. The distribution of ice and permafrost on and beneath the land and lagoon is the primary factor determining the fate and vulnerability of the coastal carbon pool and the stability of coastlines, including Kaktovik's.

The Arctic coastal plain in the area around Kaktovik is characterized by low-relief tundra underlain by continuous permafrost. The area's coast is similar to most of the northeastern Arctic coast of Alaska and northwestern Canada, which is lined with hundreds of kilometers of shallow lagoons bounded by barrier island systems (15); Kaktovik Lagoon is one of many such systems. Kaktovik Lagoon is covered with ice that is ~1.7 to 1.8 m thick 9 months of the year. The lagoon freezes down to its bottom only at shore; the rest of the lagoon has unfrozen hypersaline bottom waters during winter (16). The lagoon has an average depth of 2.5 m with a maximum of about ~4 m; many areas of the lagoon have depths ~3 m. The mean annual temperature of the lagoon bottom water varies from 0.36° to 0.43°C (16). The landward shores of Kaktovik Lagoon have narrow sandy beaches, typically a few meters wide, which abut bluffs that vary in height but are typically 1 to 3 m high (see Fig. 1 and fig. S1). The bluffs mark the beginning of the tundra with ice-wedge polygons. Ice-bonded permafrost within the polygons typically begins within a few decimeters beneath the surface. The boundaries of the polygons represent troughs that form a locally connected network of surface channels (e.g., fig. S1B), which drains groundwater from the polygons and delivers them to the beaches over the summer (i.e., August).

Freshwater enters Kaktovik Lagoon via three main mechanisms: (i) streams from the tundra, which drain small thermokarst ponds and the very local networks of troughs in between ice-wedge polygons; (ii) two relatively larger streams on the southwestern and southeastern corners of the lagoon, which include a larger drainage area; and (iii) groundwater flowing through interstices in surficial and deep porous soils, which extends into thawing permafrost and

Copyright © 2020
The Authors, some
rights reserved;
exclusive licensee
American Association
for the Advancement
of Science. No claim to
original U.S. Government
Works. Distributed
under a Creative
Commons Attribution
NonCommercial
License 4.0 (CC BY-NC).

¹Department of Geological Sciences, The University of Texas at Austin, Austin, TX 78712, USA. ²Marine Science Institute, The University of Texas at Austin, Austin, TX 78373, USA.
*Corresponding author. Email: mpedrazash@utexas.edu

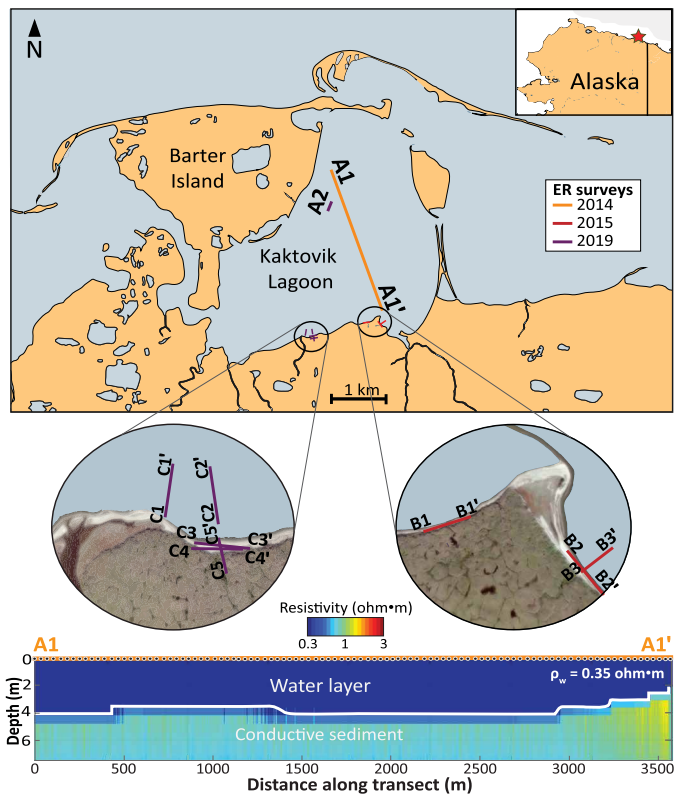


Fig. 1. Overview of the study site and locations of ER survey lines. The figure shows the location of Kaktovik Lagoon (inset) and the positions of a boat-towed marine ERI (A1) survey conducted in 2014, two terrestrial (B1 and B2) and one underwater (B3) ERI surveys conducted in 2015, and three terrestrial (C3, C4, and C5) and three underwater (A2, C1, and C2) ER surveys conducted in 2019. The bottom panel shows the inverted tomogram for survey transect A1-A1' with water layer fixed at 0.35 ohm-m, bathymetry data (white line), and logarithmic color intervals.

carries abundant dissolved organic carbon and nitrogen (17). Kaktovik Lagoon is connected with the Beaufort Sea via a narrow opening between barrier islands. However, water exchange with the open ocean is limited throughout the year and even more so during winter due to ice formation. This leads to the development of hypersaline conditions within the lagoon. The salty winter water is largely replaced by terrestrial runoff and lagoon ice melt during spring, although hypersaline bottom waters persist into summer in some deeper portions of the lagoon (15, 16). The shallow subsurface (below the sediment surface) consists mostly of peat around the edges of the lagoon, and unconsolidated marine and non-marine silt- to gravel-sized sediment as seen from boreholes on Barter Island (18).

Northern coastal lagoons, such as Kaktovik Lagoon, are model systems facing immediate local impacts of climate change, principally from warming water temperatures that will degrade subsea and coastal permafrost. There is an immediate need for information about the impacts of degrading subsea permafrost on the welfare, food security, land stability, cultural heritage, and economic growth of its residents (12). Like many areas of the Arctic coast, the presence and dynamics of subsea ice-bonded permafrost within Kaktovik Lagoon has not been documented. Recent regional mapping efforts using seismic surveys to constrain the seaward extent of subsea permafrost in the Alaska Beaufort Sea region begin relatively far

offshore and ignore the lagoons and nearshore zones where subsea permafrost is most vulnerable to degradation (5).

Coastal and offshore applications of electrical resistivity imaging (ERI) have emerged as a promising cost-effective geophysical method that can readily provide horizontally continuous and depth-resolved images of the electrical properties of the subsurface (19, 20). ERI injects electrical current into the subsurface through a series of electrodes while simultaneously measuring the electrical potential field. The premise is based on the ability of subsurface materials to resist current flow, essentially treating the subsurface like a network of resistors. Ice and frozen sediment impede current. They do not allow electricity to flow through as easily as unfrozen, conductive sediment. Electrical resistivity (ER) increases markedly with high ice content (21). Past studies have shown that ice-bonded permafrost usually manifests with an ER of >10 ohm-m in processed images of data from ER surveys with floating electrodes (so-called marine ER), while for ER surveys, where electrodes are affixed to the ground close to the shore, it usually manifests as >32 ohm-m in underwater ER surveys and >1000 ohm-m in land surveys (fig. S2).

Taking advantage of the electrical properties of ice and saturated frozen materials, previous ERI applications along open coastlines of the Laptev Sea and Beaufort Sea as well as in Elson Lagoon (near Utqiagvik, Alaska) revealed nearshore subsea frozen permafrost continuously connected with terrestrial permafrost, which gradually sloped to greater depths offshore (7–9, 22). Following these studies, we determined the subsurface resistivity distribution of Kaktovik Lagoon to identify the presence and extent of any ice-bonded or unfrozen sediment and fresh and saline interstitial water held by the sediment. We conducted ERI using a variety of survey configurations to develop a comprehensive map of the beach and lagoon subsurface (Fig. 1). The surveys were done along the beach, across the beach-lagoon interface, and deep within the lagoon. All surveys were done in summer (late July or August).

RESULTS

Shallow and deep ER profiles within the lagoon

Marine ERI surveys using floating electrodes conducted in summer 2014 showed that ER increased gradually from 0.35 ohm-m in the water column to 1.6 ohm-m within the lagoon sediment at the bottom of the profile. The most resistive areas around Kaktovik Lagoon were found closer toward the southwest shore (Fig. 1, section A1). The vertical gradational pattern in resistivity is notably uniform across the approximately 4-km-long transect (which crosses almost the entire lagoon), where the full extent of the profile reaches 7.5 m below the water surface and approximately 4 m below the sediment-water interface.

To extend the results from summer 2014 for depths greater than 4 m below the sediment, we conducted an underwater survey in 2019 where electrodes were placed on the water-sediment interface, which imaged down to 17 m (Fig. 2, section A2). The resistivity values within the transect ranged from 0.47 to 8.26 ohm-m. The most resistive values were found on top of the lagoon sediment with values between 3.0 and 8.26 ohm-m. Under this resistive zone was a ~ 15 -m-thick conductive region with an average resistivity of 1 ohm-m. The conductive zone persisted even in the less resolvable deeper areas of the lagoon sediment profile (i.e., the more transparent areas in Fig. 2, section A2).

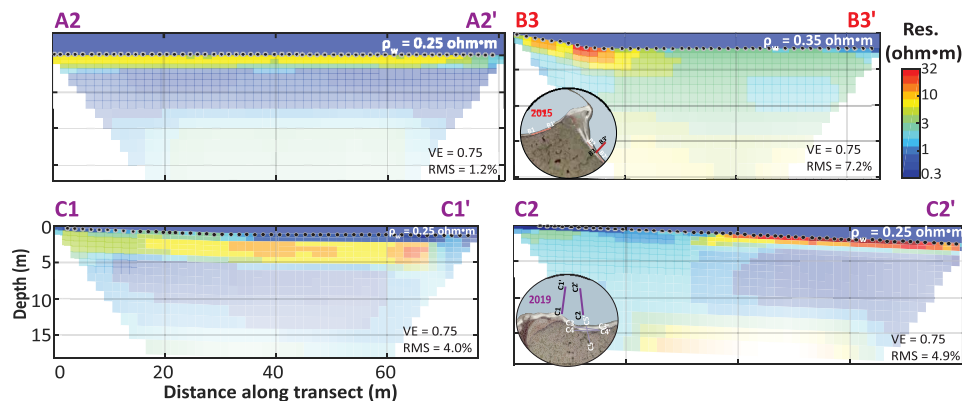


Fig. 2. Inverted tomograms for underwater ER surveys. The color intervals are logarithmic, and the model resolution of each block is denoted by its transparency. Fixed water layer resistivity was assumed in the inversion, and the resulting root mean square (RMS) error and vertical exaggeration (VE) is shown for each inversion. The location of survey transects is indicated in the inset maps. Note that line A2-A2' is located in the middle of the lagoon (see Fig. 1 for location).

An underwater ERI survey was conducted perpendicular to the beach in 2015 (Fig. 2, transect B3). The shore-perpendicular transect was at a site where suprapermafrost groundwater seeps from a thaw slump feature on the tundra (see fig. S1B). This location was chosen to image whether this fresh water infiltrates into the lagoon sediment and how this is connected with permafrost distribution. Results of the underwater ERI survey placed perpendicular to the beach (transect B3 in 2015) showed a range of resistivities from 0.6 to 35 ohm·m. There is a local resistive plume juxtaposed on top of a saline conductive region closest to the shore. The rest of the resistivity distribution is homogeneous and averages to 2.5 ohm·m, with most values <10 ohm·m.

Two more underwater ERI surveys were conducted in 2019; one (C2) was orthogonal to land surveys and another (C1) was about ~75 m to the west of line C2 (Fig. 2). Both underwater profiles were not in an area directly adjacent to a thaw slump feature, such as transect B3. These submarine surveys were done to investigate the presence or absence of ice-bonded permafrost at locations farther from shore without the complexity brought about by freshwater seeps near the land-lagoon interface. Results from the underwater ERI C2 transect showed conductive values between 1 and 3 ohm·m for the first 30-m horizontally nearshore and a thin resistive layer on top with values ~10 ohm·m further away from shore. These results were similar to transect A2, which was carried out in the middle of the lagoon. Below the resistive layer, the subsurface was homogeneous and divided into two main resistivity regions: a 30-m-wide zone with resistivity of 3 ohm·m next to a zone with a resistivity of 0.5 ohm·m. These zones show conductivity increasing away from shore. Results from the underwater ERI line C1 showed a similar pattern with a thin 1-m conductive layer on top of the more resistive ~2.5-m-thick layer across the entire transect. Below the resistive layer, the subsurface is homogeneous and conductive with resistivities <1 ohm·m until near the lowermost portions of the tomogram. The bottom of C1 and C2 showed increased resistivity; these are poorly resolved, however.

ER profiles at the shore

Terrestrial ER surveys, where electrodes were buried at the beach/soil surface, were also conducted in the summers of 2015 and 2019. The first surveys were in a southeastern section, and the latter sur-

veys were to the southwest of the lagoon. Results from both the terrestrial ER transects B1 and B2 (in the southeastern field site) exhibited increasing resistivity with depth in the upper 2 to 5 m, from the water resistivity of 0.35 ohm·m at the surface to 100 to 250 ohm·m near the bottom of this near-surface zone (Fig. 3). The more resistive zones (~200 ohm·m) were present only above 5 m depth; patches of relatively lower resistivity were also present in these shallow areas. The deeper parts of the profiles, below ~7 m depth, were uniformly conductive.

Several surveys were conducted at the southwestern coast field site. We conducted a survey along the beach (C3) that was similar to transects B1 and B2 from the southeastern side, and an additional shore-parallel survey (C4) but right next to the tundra. Results from the southwestern shore field site (C3 and C4) revealed a moderately resistive area along the shore that did not extend deeper than 7 m (Fig. 3; see C3). This zone extends to ~11 m next to the tundra-beach transition (Fig. 3, see C4), with an average resistivity of ~200 ohm·m and similar pattern to the eastern land surveys made in 2015 (B1 and B2). Below the shallow resistive area, the subsurface was conductive and fairly homogeneous.

An orthogonal survey (C5) crossing survey lines C3 and C4 from the shoreline toward the tundra with about half covering the beach and the other half covering ice-wedge polygons was also conducted. This transect went across a high-centered ice-wedge polygon where ice-bonded permafrost was found at 30 cm depth. The C5 transect allowed us to constrain the method with known ice-bonded permafrost and for mapping the distribution of the ice-bonded permafrost distribution going from the tundra toward the beach (Fig. 3). The resistivity distribution from the survey running perpendicular to the shoreline toward the tundra (C5, which crosses lines C3 and C4) varied over four orders of magnitude, ranging from less than 10 ohm·m to more than 10,000 ohm·m (Fig. 3). The most conductive areas were found in the shallow zone near the shoreline, as would be expected. However, there were some conductive areas below the highly resistive regions for the entire profile. These resistive values ranged between 1000 and 10,000 ohm·m and did not extend deeper than ~3.5 m. Although not fully resolved, the deeper subsurface below the highly resistive 3.5-m-thick layer had resistivity values ranging from 10 to <200 ohm·m. The moderately resistive values near 200 ohm·m sloped downwards toward the shore.

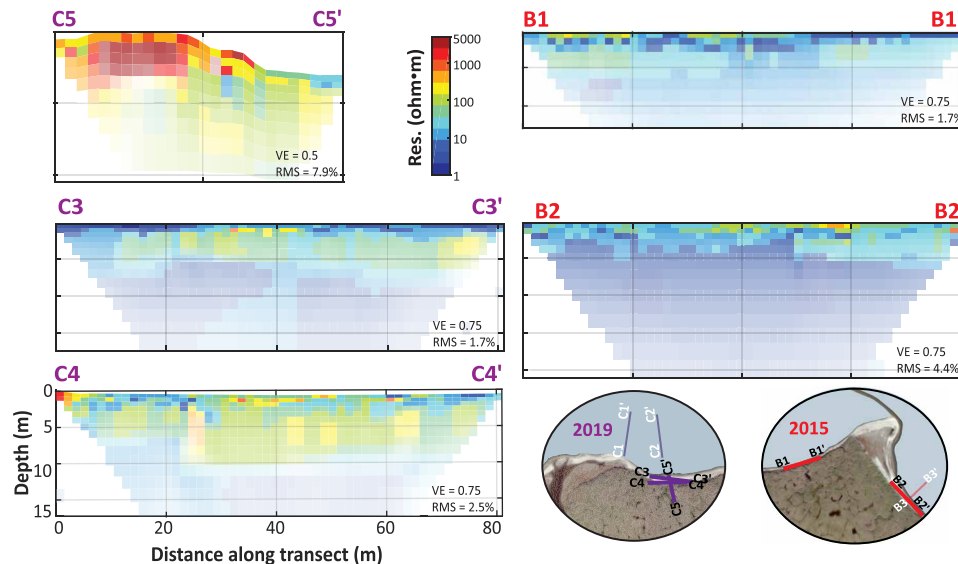


Fig. 3. Inverted tomograms for terrestrial ER surveys. The color intervals are logarithmic, and the model resolution of each block is denoted by its transparency. The resulting RMS error and VE is shown for each inversion. The location of survey transects is indicated in the inset maps.

DISCUSSION

The bulk ER of subsurface materials depends on both the solid matrix (i.e., its composition, texture, and porosity) and the material filling the voids. Unfrozen sediment that is water-saturated provides a conduit for electrical current; in addition, higher salinity and clay content enhance the capacity to transmit current (23). In contrast, frozen sediment with substantial ice saturation resists the passage of electricity. We expect ice-bonded sediment to have exponentially higher resistivity than unfrozen sediment. The resistivity of fresh water usually ranges between 10 and 500 ohm-m, whereas the resistivity of sea water is below 1 ohm-m (24).

ER surveys in aquatic and marine settings, such as transects A1, A2, C1, and C2, are liable to electrical current channeling where overlying conductive zones effectively mask resistive zones underneath because the current is focused within and does not penetrate beyond the conductive zone. Surveys with floating electrodes, such as transect A1, are particularly challenged by this. Thus, subsea ice-bonded permafrost that may have actual resistivity in the hundreds to thousands of ohm-meters will have an apparent resistivity that is lower than the actual resistivity. Forward modeling (fig. S3) and synthesis of the literature (fig. S2) show that subsea ice-bonded permafrost will nonetheless manifest with an apparent ER that is ≥ 10 ohm-m.

In Kaktovik Lagoon, water column resistivity values ranging between 0.2 and 0.5 ohm-m during the summer (Figs. 1 and 2) preclude the possibility that porewater near the sediment surface is fresh (16). Furthermore, water temperatures of 10° to 11°C (typical for Beaufort Sea lagoons during summer) cannot support near-surface permafrost (16). Thus, the moderately resistive values encountered near the sediment surface must be explained by other factors. Surficial sediment samples collected near section C2 ranged in size from that of silt to gravel, but in some cases, both sediment class sizes were found together. It is therefore likely that elevated resistivity in the top few meters of sections C1, C2, and most likely A2 is a consequence of a sedimentological change from relatively resistive gravel and sands to more conductive silts and even muds rather than a

pore fluid phase change. In any case, lower resistivity values throughout much of our ER depth range (< 10 ohm-m; A1 in Fig. 1 and A2 in Fig. 2) suggest that the area encompassing much of the lagoon is free of ice-bonded permafrost down to at least 17 m.

Moderate increases in resistivity toward the bottom of C1 and C2 could be indicative of ice-bearing sediments; however, the resistivity values in these areas are at the lower end of what we would expect for ice-bonded permafrost, and the areas are not well resolved. While the poor resolution could be attributed to the depth (i.e., at the deepest portions of the tomogram), it could also result from current channeling. The more resistive features near the lower end of the depth range could be due to the presence of some ice or colder temperatures or both. ER lines A2 and B3 also exhibited higher resistivity at their deepest extent. However, the resistivity values along these transects remained < 10 ohm-m, less than what is the expected apparent ER for ice-bonded permafrost.

The tomograms of the terrestrial ER surveys along the beach had resistivity values < 1000 ohm-m for all surveys except C5 and the first two electrodes of C4. Given the ~ 10 -m spacing between the relatively parallel lines C3 and C4, we can assume that the lithology remains more or less uniform. An observation of the lithology made by digging shallow holes on the beach supports this assertion. Therefore, the increase in shallow resistivity closer to the tundra can be attributed to a difference in pore water salinity or temperature (compare the parallel lines C3 and C4 in Fig. 3). This suggests that there exists an annulus of fresher and/or colder water along the lagoon coast derived from the tundra. Our resistivity measurement from beneath the beach matches more closely with that of fresh water extracted from the channel between ice-wedge polygons (43 ohm-m) than the lagoon water's resistivity (0.35 ohm-m). Thus, this further supports the hypothesis that groundwater along the beach is sourced from the tundra. The shallow (topmost) resistive areas in the tomograms roughly coincided with where fresher water was observed in co-located boreholes (fig. S4). The only possible source of this fresh water is the suprapermast zone (or active layer) on land. This water may be delivered as direct subsurface seepage or

as channelized flows from the polygon troughs. The channels draining the polygons were found to sometimes drain directly into the lagoon (e.g., the channel shown in fig. S1B), disappear and infiltrate into the beach sediment, or form puddles (see top of picture in fig. S1A; transects C3 and C4 end at this puddle). We surmise that these freshwater bodies and conveyors intermittently transition from one state to the other, depending on tidal, wave, and hydro-climatic conditions.

Nearer the lagoon water line, resistivity decreased toward that typical of saline water-saturated unfrozen sediment. The only tomogram that indicated extensive ice-bonded permafrost is line C5, which started on the tundra, cut across a high-centered ice-wedge polygon and then continued to the beach until the water line. In this transect, the ice is obvious with a strong contrast between unfrozen and frozen material with an ER of >1000 ohm-m and reaching values $>10,000$ ohm-m. The frost table was detected at around 30 cm depth in the polygon. This transect captured the ice disappearing laterally not only at the beach but also vertically under the polygon on land. Ice was also detected at the edge of C4; the first electrode of C4 (to the west; see fig. S4D) was placed on top of the coastal bluff where direct probing indicated ice.

Forward modeling was conducted to interpret C5 (fig. S5). The results of this analysis indicate that the low resistivity region under the frozen zone of the ice-wedge polygon is not an artifact of the ER survey design or the postprocessing. The inverted tomograms of the field ER surveys are consistent with the absence of ice or ice-bonded soil under the polygon.

Our results do not show values that are reflective of massive ice or ice-bonded permafrost (8, 9, 20, 22, 24–27). The absence of ice-bonded permafrost within the lagoon and along the coast, even

below the known ice in the case of transect C5, implies that the unfrozen, water-saturated substrate under the lagoon continues under the thin ice-bonded permafrost body (Fig. 4). However, this does not preclude the presence of ice-bearing (but not ice-bonded) permafrost, which can have a resistivity of <10 ohm-m (8, 28). Regional ice-bonded permafrost extends everywhere offshore along the Arctic coast up to the 25-m isobath, which is within 37 km from land (5). Within a few kilometers offshore, including areas with lagoons, the top of the ice-bonded permafrost is, on average, 170 to 195 m below sea level (29, 30). In some places, the top is found at the surface; in others, it could be as deep as 470 m. Shallower ice tables tend to be present near barrier islands or river outlets (29). Subsea ice-bonded permafrost is normally 100 to 500 m thick (29). The ice-bonded permafrost on land in nearby Prudhoe Bay is ~ 600 m thick (31). Thus, Kaktovik Lagoon is expected to be underlain by ice-bonded permafrost at greater depths. A gradual and quasi-linear deepening of the ice table has been shown for other lagoons and coastal areas. At Elson Lagoon near Utqiagvik, Alaska, it was shown through ER measurements that the ice table deepens from the beach going lagoonward; the ice table is typically less than 5 m deep within 100 m of the shore (8). In these studies, no ice was detected in the 12-m-deep tomograms about 1 km away from shore. In the Bykovsky Peninsula, in Siberia, the ice-bonded permafrost table was detected at 16.7 m depth below the seabed 350 m from shore (9). The slope of the ice table was found to be 0.0044 near Prudhoe Bay, which suggests a deepening of 0.44 m per 100-m distance from shore (32). Thus, ice-free shallow lagoon sediment, i.e., marine talik, is not entirely unexpected. Marine talik may have variable depths and thicknesses depending on the history of the lagoon-barrier island system. Our observations are unexpected and vastly differ

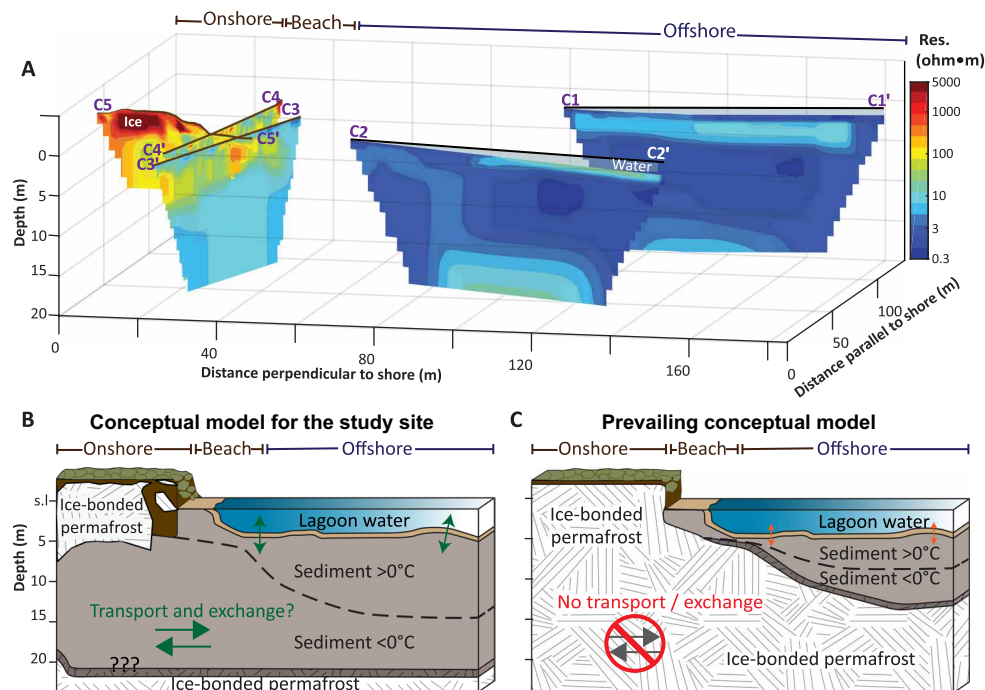


Fig. 4. Conceptual model based on the study's results. (A) Tomograms based on observations acquired in 2019 from the southwestern site (C transects). (B) Conceptual interpretation following (A) where there is an extensive talik under the lagoon and the beach, possibly extending further in-land through connection with a potential cryopeg. (C) Prevailing conceptual model for subsea permafrost where it is connected to terrestrial ice-bonded permafrost. The models depict the long-term summer state of the lagoons.

from other studies in that the ice table gets deep rapidly, down to >22 m right at the beach.

We hypothesize four potential explanations for the extensive talik under the lagoon. First, there was not any ice to begin with in the deeper subsurface, but rather, it represents an ancient cryopeg, essentially a high salinity talik, which was never frozen due to the freezing point depression of hypersaline interstitial water within fine-grained sediment. This would be similar to resistivity observations (8 to 20 ohm-m) of subsurface brines in Utqiagvik, Alaska (26, 33). Second, the ice imaged in the ice-wedge polygons, which may have extended into and through the lagoon in the past, has thawed abruptly, resulting in land subsidence, which is controlled by timing that is difficult to constrain (34). Third, the ice has been continually thawing at a relatively high rate over a long period of time. That is, the thaw front is more or less at the coast and moving all the time with the coast as it erodes. Fourth, the thawed area is a relict talik of a thermokarst lake that became connected with the coast to form a thermokarst lagoon (35).

Our results cannot definitively show which of these hypotheses is correct. However, some constraints are possible based on known ranges for coastal erosion and ice table deepening. Taking a coastal erosion rate of 0.6 m/year (14), the average for Kaktovik Lagoon's coast, 60 m of land would submerge in a century. Where the coast was at the start of that century, the ice table would deepen by 4 m if one assumes the average subsea permafrost degradation of 4 cm/year in the Alaskan Beaufort Sea (7, 8). Rates of ice table deepening could have been higher in the lagoons because summer temperatures are greater inside the lagoons compared to open coastal waters. Nonetheless, based on these rough calculations, vertical thawing of 17+ m of ice-bonded relict permafrost at a rate that matches shoreline retreat seems improbable, and abrupt thawing over a shorter period is even less likely. The remaining two hypotheses are harder to separate. Thermokarst lakes are a common feature within the coastal plain of northern Alaska, and it is certainly possible that taliks associated with former lakes persist as lagoons shift landward with coastal erosion. However, a cryopeg beneath the tundra would also persist as lagoons shift landward. An unfrozen brine-rich layer associated with ancient marine-derived sediments has been well documented beneath the tundra near Utqiagvik (36, 37), and we suspect that the unfrozen layer beneath transect C5 is a similar manifestation.

Regardless of its origin, our study reveals that there is an extensive talik across the entire lagoon connected to a subpermafrost aquifer (cryopeg) where saline groundwater has the potential to mix with fresh water from thawing ice polygons and incoming freshwater channels. We acknowledge that the extent, depth, and amount or degree of this mixture is unknown and requires further investigation. Nonetheless, organic matter in the talik aquifer/lagoon sediment is now liberated and free to react and escape as gases or get transported as dissolved organic matter. Measurements along the landward margin of Kaktovik Lagoon indicate that suprapermafrost groundwater contains very high concentrations of dissolved organic matter (17). Organic matter from suprapermafrost and subsea permafrost groundwater inputs could be mineralized and released as carbon dioxide or methane or incorporated into lagoon biota, thereby providing a source of greenhouse gas emissions that constitute a positive feedback to warming or a source of energy for lower trophic productivity in the lagoons. These processes may be critical for the hydrologic, biogeochemical, and ecological func-

tioning of the lagoon-barrier island system at present and into the future.

ERI is an excellent method for determining the extent of thawed sediment versus ice-bonded permafrost across the land to lagoon interface. Detection of potential changes in coastal subsea permafrost extent will provide very valuable information on thawing at a critical and potentially rapidly changing zone where terrestrial and marine processes are interlinked. This information is needed to comprehensively connect climate change and its impacts on lagoon ecosystems in the Arctic.

MATERIALS AND METHODS

Marine ER measurements

In August 2014, we used a SuperSting R8 eight-channel ERI system from Advanced Geosciences Inc. (AGI) to acquire approximately 4 km of marine ERI data (Fig. 1). We used a dipole-dipole array with floating electrodes towed behind a small boat (fig. S1C). The potential electrodes were noncorrosive passive graphite electrodes 7 cm in length and 2.5 cm in diameter. The injection electrodes were stainless steel tubes of ~25 cm length and 5 cm diameter. The electrode spacing was 3 m along the streamer, and voltage was measured using 10 pairings of electrodes. Electrode position was determined real-time using an onboard GPS, and water depth was measured using an echo sounder. The injected electrical current and the electrode pair potentials were measured and recorded continuously at intervals of at least 1 m as the array was towed. At the same time as the marine ERI survey, the sea layer resistivity was measured in the beach to be 0.27 ohm-m using a handheld conductivity meter; this is similar to values reported in (16) for the center of Kaktovik Lagoon during August for the years 2011, 2012, and 2013, which averaged to 0.35 ohm-m. This survey is referred to as "marine ER."

Terrestrial ER measurements

A set of fixed electrode ERI surveys was conducted in August 2015 (Fig. 1 and fig. S1), where electrodes were buried in the sediment in the southeastern field site. Two ERI surveys parallel to the beach shore were carried out using both a dipole-dipole array and a Schlumberger array with a 1.5-m spacing for a total length of 82.5 m. In August 2019, two ERI surveys parallel to the beach shore and one orthogonal to the shore were carried out using the dipole-dipole electrode array with 1.5-m spacing in the southwestern field site (Fig. 1 and fig. S4). Topographic data were acquired using a portable laser theodolite to constrain the inversion. These are referred to as "terrestrial ER."

Underwater ER measurements

One underwater ERI survey was conducted perpendicular to the coast in 2015 and three in 2019—these are referred to as "underwater ERI." The electrodes were set on the seabed using lead weights, and only observations from the submerged electrodes fixed on the sea bed were analyzed. The dipole-dipole and Schlumberger surveys from 2015 were combined into one dataset before inversion. The sea layer resistivity was determined to be 0.25 ohm-m using a handheld fluid electrical conductivity probe, and the topographic data were acquired using a portable laser theodolite. On a few occasions, we directly probed for the frost table within the underwater ER transects using a 3.65-m-long folding aluminum rod (an avalanche probe) but did not encounter any hard materials.

Inversion of ER survey data

All underwater and terrestrial inversions were implemented using the software RES2DINV (38) to invert the apparent resistivity data using a robust or blocky inversion method (39) because we expected potentially sharp boundaries if ice-bonded permafrost was present. The marine ERI boat-towed floating electrodes data were inverted using AGI EarthImager 2D Software whose inversion settings were similar to those used in RES2DINV to the extent possible. Inversion continued until the root mean square (RMS) error between subsequent iterations was <5%, usually between three and seven iterations. The sea layer resistivity was fixed for the marine and underwater ERI surveys based on field data. The inversion parameters can be found in table S1. Inversion performance was indicated by the RMS error between the field apparent resistivity measurements and the apparent resistivity data calculated from the inverted model.

ER model resolution

To quantify how well ER is able to resolve a feature at a given depth, we quantified the model “resolution” values following the model resolution equation that relates the calculated model resistivity, q_{Model} , to the true resistivity, q_{True} (40). This essentially treats the resolution matrix, R , as a filter through which the inversion method attempts to resolve the subsurface resistivity. R is defined as

$$R = q_{\text{Model}}/q_{\text{True}}$$

In general, the resolution is greatest near the surface where the electrodes are placed and rapidly decreases with depth. Here, we used the resolution matrix to control the transparency of the data blocks, making the lower resolution values more transparent and the higher resolution values more opaque. In addition, we applied an edge filter with a slope of 1:1 to blank out data in the edges where current is less likely to penetrate and thus where data are unreliable.

Forward modeling of ER surveys

Forward modeling was conducted to further interpret transects A1 (marine ER) and C5 (terrestrial ER). The forward modeling was conducted with RES2DMOD. For the marine ER forward modeling, the “actual” ER configuration included a permafrost layer beneath seawater and unfrozen sediment. The permafrost resistivity was increased across the broad range of 30 to 300,000 ohm-m. The synthetic ER fields were then synthetically surveyed following the same design as the boat-towed survey of A1 and inverted similarly as A1 using RES2DINV. For interpreting C5, two synthetic ER fields (the actual hypothetical fields) were constructed with three ER units representing ice-bonded permafrost (5000 ohm-m), unfrozen salt water-saturated or fine grain sediment (20 ohm-m), and relatively fresh water-saturated or coarse grain sediment (200 ohm-m). The hypothetical ER fields were then synthetically surveyed following the same dipole-dipole design as the field surveys. The resulting synthetic survey data were inverted following the same protocol used for inverting the real field data using RES2DINV. The forward modeling design and results are presented in figs. S3 and S5.

Salinity measurements along the ER lines

For one of the terrestrial ERI survey lines (Fig. 3, transect C3), six holes were dug at different intervals along the line to investigate whether the pore water resistivity correlated to the shallow sediment resistivity. Holes were dug to a depth of ~50 cm using a shovel, and

water from the sediment was allowed to fill in the hole before testing for its resistivity using a handheld fluid electrical conductivity probe (see fig. S4).

SUPPLEMENTARY MATERIALS

Supplementary material for this article is available at <http://advances.sciencemag.org/cgi/content/full/6/43/eabb5083/DC1>

REFERENCES AND NOTES

1. A. Lindgren, G. Hugelius, P. Kuhry, T. R. Christensen, J. Vandenberghe, GIS-based maps and area estimates of northern hemisphere permafrost extent during the Last Glacial Maximum. *Permafrost. Periglac. Process.* **27**, 6–16 (2016).
2. J. E. Vonk, L. Sánchez-García, B. E. van Dongen, V. Alling, D. Kosmach, A. Charkin, I. P. Semiletov, O. V. Dudarev, N. Shakhova, P. Roos, T. I. Eglinton, A. Andersson, Ö. Gustafsson, Activation of old carbon by erosion of coastal and subsea permafrost in Arctic Siberia. *Nature* **489**, 137–140 (2012).
3. A. Lindgren, G. Hugelius, P. Kuhry, Extensive loss of past permafrost carbon but a net accumulation into present-day soils. *Nature* **560**, 219–222 (2018).
4. A. Portnov, A. J. Smith, J. Miener, G. Cherkashov, P. Rekan, P. Semenov, P. Serov, B. Vanshtein, Offshore permafrost decay and massive seabed methane escape in water depths >20 m at the South Kara Sea shelf. *Geophys. Res. Lett.* **40**, 3962–3967 (2013).
5. L. L. Brothers, B. M. Herman, P. E. Hart, C. D. Ruppel, Subsea ice-bearing permafrost on the U.S. Beaufort Margin: 1. Minimum seaward extent defined from multichannel seismic reflection data. *Geochem. Geophys. Geosyst.* **17**, 4354–4365 (2016).
6. P. P. Overduin, T. S. von Deimling, F. Miesner, M. N. Grigoriev, C. Ruppel, A. Vasiliev, H. Lantuit, B. Juhs, S. Westermann, Submarine permafrost Map in the arctic modeled using 1-D transient heat flux (SuPerMAP). *J. Geophys. Res. Oceans* **124**, 3490–3507 (2019).
7. N. Shakhova, I. Semiletov, O. Gustafsson, V. Sergienko, L. Lobkovsky, O. Dudarev, V. Tumskey, M. Grigoriev, A. Mazurov, A. Salyuk, R. Ananiev, A. Koshurnikov, D. Kosmach, A. Charkin, N. Dmitrevsky, V. Karnaukh, A. Gunar, A. Meluzov, D. Chernykh, Current rates and mechanisms of subsea permafrost degradation in the East Siberian Arctic Shelf. *Nat. Commun.* **8**, 15872 (2017).
8. P. P. Overduin, S. Westermann, K. Yoshikawa, T. Haberlau, V. Romanovsky, S. Wetterich, Geoelectric observations of the degradation of nearshore submarine permafrost at Barrow (Alaskan Beaufort Sea). *J. Geophys. Res. Earth* **117**, F02004 (2012).
9. M. Angelopoulos, S. Westermann, P. Overduin, A. Faguet, V. Olenchenko, G. Grosse, M. N. Grigoriev, Heat and salt flow in subsea permafrost modeled with CryoGRID2. *J. Geophys. Res. Earth Surf.* **124**, 920–937 (2019).
10. C. D. Ruppel, J. D. Kessler, The interaction of climate change and methane hydrates. *Rev. Geophys.* **55**, 126–168 (2017).
11. G. Hugelius, J. Strauss, S. Zubrzycki, J. W. Harden, E. A. G. Schuur, C.-L. Ping, L. Schirmer, G. Grosse, G. J. Michaelson, C. D. Koven, J. A. O'Donnell, B. Elberling, U. Mishra, P. Camill, Z. Yu, J. Palmtag, P. Kuhry, Estimated stocks of circumpolar permafrost carbon with quantified uncertainty ranges and identified data gaps. *Bioosciences* **11**, 6573–6593 (2014).
12. M. Fritz, J. E. Vonk, H. Lantuit, Collapsing Arctic coastlines. *Nat. Clim. Change* **7**, 6–7 (2017).
13. T. E. Osterkamp, *Encyclopedia of Ocean Sciences* (Elsevier, 2001), vol. 5, pp. 2902–2912.
14. A. E. Gibbs, B. M. Richmond, “National assessment of shoreline change—Summary statistics for updated vector shorelines and associated shoreline change data for the north coast of Alaska, U.S.–Canadian Border to Icy Cape” (Open-File Report, U.S. Geological Survey, 2017).
15. K. H. Dunton, S. V. Schonberg, L. W. Cooper, Food web structure of the Alaskan nearshore shelf and estuarine lagoons of the beaufort sea. *Estuaries Coast* **35**, 416–435 (2012).
16. C. M. Harris, J. W. McClelland, T. L. Connelly, B. C. Crump, K. H. Dunton, Salinity and temperature regimes in Eastern Alaskan beaufort sea lagoons in relation to source water contributions. *Estuaries Coasts* **40**, 50–62 (2017).
17. C. T. Connolly, M. B. Cardenas, G. A. Burkart, R. G. M. Spencer, J. W. McClelland, Groundwater as a major source of dissolved organic matter to Arctic coastal waters. *Nat. Commun.* **11**, 1479 (2020).
18. T. E. Osterkamp, J. C. Jorgenson, Warming of permafrost in the Arctic National Wildlife Refuge, Alaska. *Permafrost. Periglac. Process.* **17**, 65–69 (2006).
19. M. B. Cardenas, P. B. Zamora, F. P. Siringan, M. R. Lapus, R. S. Rodolfo, G. S. Jacinto, M. L. San Diego-McGlone, C. L. Villanoy, O. Cabrera, M. I. Senal, Linking regional sources and pathways for submarine groundwater discharge at a reef by electrical resistivity tomography, ^{222}Rn , and salinity measurements. *Geophys. Res. Lett.* **37**, (2010).
20. P. W. Swarzenski, C. D. Johnson, T. D. Lorenson, C. H. Conaway, A. E. Gibbs, L. H. Erikson, B. M. Richmond, M. P. Waldrop, Seasonal electrical resistivity surveys of a coastal bluff, Barter Island, North Slope Alaska. *J. Environ. Eng. Geophys.* **21**, 37–42 (2016).
21. C. F. Pearson, P. M. Halleck, P. L. McGuire, R. Hermes, M. Mathews, Natural gas hydrate deposits: A review of in situ properties. *J. Phys. Chem.* **87**, 4180–4185 (1983).

22. P. P. Overduin, S. Wetterich, F. Günther, M. N. Grigoriev, G. Grosse, L. Schirmermeister, H. W. Hubberten, A. Makarov, Coastal dynamics and submarine permafrost in shallow water of the central Laptev Sea, East Siberia. *Cryosphere* **10**, 1449–1462 (2016).
23. R. Fortier, M. Allard, M.-K. Seguin, Effect of physical properties of frozen ground on electrical resistivity logging. *Cold Reg. Sci. Technol.* **22**, 361–384 (1994).
24. M. Kasprzak, M. C. Strzelecki, A. Traczyk, M. Kondracka, M. Lim, K. Migala, On the potential for a bottom active layer below coastal permafrost: The impact of seawater on permafrost degradation imaged by electrical resistivity tomography (Hornsund, SW Spitsbergen). *Geomorphology* **293**, 347–359 (2017).
25. P. V. Sellmann, A. J. Delaney, S. A. Arcone, *Coastal Subsea Permafrost and Bedrock Observations Using Dc Resistivity* (Cold Regions Research and Engineering Lab, 1989).
26. K. Yoshikawa, V. E. Romanovsky, N. Duxbury, J. Brown, A. Tsapin, The use of geophysical methods to discriminate between brine layers and freshwater. *J. Glaciol. Geocryol.* **26**, 301–309 (2004).
27. S. S. Hubbard, C. Gangogadagamage, B. Dafflon, H. Wainwright, J. Peterson, A. Gusmeroli, C. Ulrich, Y. Wu, C. Wilson, J. Rowland, C. Tweedie, S. D. Wulfschleger, Quantifying and relating land-surface and subsurface variability in permafrost environments using LiDAR and surface geophysical datasets. *Hydrogeol. J.* **21**, 149–169 (2013).
28. Y. Wu, S. Nakagawa, T. J. Kneafsey, B. Dafflon, S. Hubbard, Electrical and seismic response of saline permafrost soil during freeze-thaw transition. *J. Appl. Geophys.* **146**, 16–26 (2017).
29. D. Sherman, S. C. Constable, Permafrost extent on the Alaskan Beaufort shelf from surface-towed controlled-source electromagnetic surveys. *J. Geophys. Res. Solid Earth* **123**, 7253–7265 (2018).
30. L. L. Brothers, P. E. Hart, C. D. Ruppel, Minimum distribution of subsea ice-bearing permafrost on the U.S. Beaufort Sea continental shelf. *Geophys. Res. Lett.* **39**, L15501 (2012).
31. T. E. Osterkamp, M. W. Payne, Estimates of permafrost thickness from well logs in northern Alaska. *Cold Reg. Sci. Technol.* **5**, 13–27 (1981).
32. T. E. Osterkamp, G. C. Baker, W. D. Harrison, T. Matava, Characteristics of the active layer and shallow subsea permafrost. *J. Geophys. Res. Oceans* **94**, 16227–16236 (1989).
33. J. Brown, *Ionic Concentration Gradients in Permafrost, Barrow, Alaska* (Cold Regions Research and Engineering Lab, 1969).
34. K. Walter Anthony, T. Schneider von Deimling, I. Nitze, S. Frolking, A. Emond, R. Daanen, P. Anthony, P. Lindgren, B. Jones, G. Grosse, 21st-century modeled permafrost carbon emissions accelerated by abrupt thaw beneath lakes. *Nat. Commun.* **9**, 3262 (2018).
35. L. Schirmermeister, M. N. Grigoriev, J. Strauss, G. Grosse, P. P. Overduin, A. Kholodov, F. Guenther, H. W. Hubberten, Sediment characteristics of a thermokarst lagoon in the northeastern Siberian Arctic (Ivashkina Lagoon, Bykovsky Peninsula). *Ark. Dent.* **4**, 13 (2018).
36. B. Dafflon, S. Hubbard, C. Ulrich, J. Peterson, Y. X. Wu, H. Wainwright, T. J. Kneafsey, Geophysical estimation of shallow permafrost distribution and properties in an ice-wedge polygon-dominated Arctic tundra region. *Geophysics* **81**, Wa247–Wa263 (2016).
37. H. Meyer, L. Schirmermeister, A. Andreev, D. Wagner, H. W. Hubberten, K. Yoshikawa, A. Bobrov, S. Wetterich, T. Opel, E. Kandiano, J. Brown, Lateglacial and Holocene isotopic and environmental history of northern coastal Alaska – Results from a buried ice-wedge system at Barrow. *Quaternary Sci. Rev.* **29**, 3720–3735 (2010).
38. M. H. Loke, R. D. Barker, Rapid least-squares inversion of apparent resistivity pseudosections by a quasi-Newton method. *Geophys. Prospect.* **44**, 131–152 (1996).
39. J. F. Claerbout, F. Muir, Robust modeling with erratic data. *Geophysics* **38**, 826–844 (1973).
40. F. D. Day-Lewis, K. Singha, A. M. Binley, Applying petrophysical models to radar travel time and electrical resistivity tomograms: Resolution-dependent limitations. *J. Geophys. Res. Solid Earth* **110**, B08206 (2005).

Acknowledgments: We are grateful to the Kaktovik Inupiat Corporation for permitting us to carry out field work on their land. We thank the U.S. Fish and Wildlife Service for logistical support and for permits to conduct research within the lagoon. **Funding:** This work was supported by the Geology Foundation at the University of Texas at Austin. Resources were provided by the National Science Foundation through the Beaufort Lagoon Ecosystems LTER (award no. 1656026). M.N.P. was supported by a fellowship from the Ivanhoe Foundation and a student research grant from the Geological Society of America. **Author contributions:** M.N.P., M.B.C., and J.W.M. designed the study. All authors conducted field work. M.N.P. analyzed the resistivity data, created the figures, and wrote the manuscript with guidance from M.B.C. All authors provided input during the writing of the manuscript. **Competing interests:** The authors declare that they have no competing interests. **Data and materials availability:** All data have been uploaded to figshare: https://figshare.com/projects/Absence_of_ice-bonded_permafrost_beneath_an_Arctic_lagoon/80042.

Submitted 29 February 2020
 Accepted 11 September 2020
 Published 23 October 2020
 10.1126/sciadv.abb5083

Citation: M. N. Pedrazas, M. B. Cardenas, C. Demir, J. A. Watson, C. T. Connolly, J. W. McClelland, Absence of ice-bonded permafrost beneath an Arctic lagoon revealed by electrical geophysics. *Sci. Adv.* **6**, eabb5083 (2020).

Absence of ice-bonded permafrost beneath an Arctic lagoon revealed by electrical geophysics

Micaela N. Pedrazas, M. Bayani Cardenas, Cansu Demir, Jeffery A. Watson, Craig T. Connolly and James W. McClelland

Sci Adv **6** (43), eabb5083.

DOI: 10.1126/sciadv.abb5083

ARTICLE TOOLS

<http://advances.sciencemag.org/content/6/43/eabb5083>

SUPPLEMENTARY MATERIALS

<http://advances.sciencemag.org/content/suppl/2020/10/19/6.43.eabb5083.DC1>

REFERENCES

This article cites 35 articles, 2 of which you can access for free
<http://advances.sciencemag.org/content/6/43/eabb5083#BIBL>

PERMISSIONS

<http://www.sciencemag.org/help/reprints-and-permissions>

Use of this article is subject to the [Terms of Service](#)

Science Advances (ISSN 2375-2548) is published by the American Association for the Advancement of Science, 1200 New York Avenue NW, Washington, DC 20005. The title *Science Advances* is a registered trademark of AAAS.

Copyright © 2020 The Authors, some rights reserved; exclusive licensee American Association for the Advancement of Science. No claim to original U.S. Government Works. Distributed under a Creative Commons Attribution NonCommercial License 4.0 (CC BY-NC).